Diamond & Related Materials 168 (2026) 113985

Contents lists available at ScienceDirect

Diamond & Related Materials

journal homepage: www.elsevier.com/locate/diamond

A novel FeO-terminated diamond surface: Synthesis and characterization for negative electron affinity

Ettore Mingardo [a], Ramiz Zulkharnay [b], Mattia Cattelan [a,c,d,*]

[a] Department of Chemical Science, University of Padova, Padova, 3513, Italy
[b] School of Chemistry, University of Bristol, Cantock's Close, Bristol, BS8 1TS, UK
[c] INSTM Istituto Nazionale Scienza e Tecnologia dei Materiali, Padova Research Unit, Firenze, 50121, Italy
[d] CIRCC Consorzio Interuniversitario per le Reattività Chimiche e la Catalisi, Padova Research Unit, Bari, 70126, Italy

ARTICLE INFO

Keywords:
Diamond
Oxidation
Metallization
Surface functionalization
Negative electron affinity

ABSTRACT

Realizing stable negative electron affinity (NEA) in diamond remains a key challenge for electron emission and related applications. Here, we present a strategy to form a novel FeO-terminated diamond surface, enabling controlled tuning of its electronic structure. The chemical and electronic properties of the resulting interface were investigated using core-level and valence band photoemission spectroscopy. Iron preferentially reacts with surface hydroxyl groups, forming

an Fe^{2+} oxide layer and generating Fe–O–C interfacial dipoles that drive the transition of the diamond surface from positive to NEA. The behaviour of the system as a function of Fe coverage reveals a saturation regime, with optimal modification achieved at ~1 monolayer equivalent, where the work function is reduced to 4.2 eV, and the NEA reaches −0.4 eV. Notably, valence band photoemission provides the first evidence of well-defined oxide-specific Fe 3*d* states in this class of metal-based terminations, demonstrating the formation of a semiconductor-semiconductor interface. These findings establish FeO-terminated diamond as a promising platform for electronic, electron emission, and photocatalytic applications.

1. Introduction

Diamond has attracted considerable interest as an advanced material because of its outstanding mechanical strength, high thermal conductivity, and unique electronic characteristics [1]. As a result, continuous research has significantly broadened its range of applications, especially in energy conversion technologies. In this context, diamond has been widely investigated as a low work function (WF) cathode in thermionic energy converters (TECs), where thermionic emission enables higher efficiencies compared to conventional photovoltaic systems [2–4]. Beyond energy conversion, diamond has also found applications in a variety of electronic and optoelectronic systems, including secondary electron emission devices [5], field effect transistors (FETs) [6], and cold cathodes [7]. Moreover, diamond can act as a solid-state source of solvated electrons [8], facilitating a wide range of crucial reduction reactions [8–10].

A common feature underlying these diverse applications is the negative electron affinity (NEA) exhibited by diamonds with specific surface terminations. NEA is an exceptional condition in which the vacuum level lies below the conduction band minimum (CBM), such that electrons at the CBM can be emitted into vacuum without an energy barrier, corresponding to an effectively reduced WF [9,11]. Wide band-gap materials like AlN [12], c-BN [13] and, most notably, diamond [14,15] are known to exhibit this property.

The formation of NEA in diamond is strongly governed by surface dipoles. Among the various terminations studied to date, hydrogen-terminated diamond exhibits some of the lowest NEA values [16–19]. In this case, the C—H bond induces a surface dipole oriented outward due to the higher electronegativity of carbon compared to hydrogen [20]. However, hydrogen-terminated surfaces suffer from poor stability as hydrogen can desorb, and the surface readily oxidizes under air exposure or thermal and photon-induced excitation [11,19] This instability leads to degradation in device performance, limiting practical applications.

In contrast, oxygen-terminated diamond surfaces are significantly more stable. These systems have been shown to withstand prolonged air exposure and annealing at temperatures exceeding 700 °C under ultra-high vacuum (UHV) conditions [21]. Oxygen termination can be

* Corresponding author at: Department of Chemical Science, University of Padova, Padova, 3513, Italy.
E-mail address: mattia.cattelan@unipd.it (M. Cattelan).

https://doi.org/10.1016/j.diamond.2026.113985
Received 17 April 2026; Received in revised form 7 July 2026; Accepted 15 July 2026
Available online 21 July 2026

achieved through various methods, including wet chemical oxidation in strong acids, oxygen plasma treatment, and UV-assisted ozone processing [22–24]. However, oxidation typically results in increased surface roughness and non-uniform WF distribution. [22,25–27] More importantly, oxygen termination reverses the surface dipole orientation, shifting the WF above the CBM, thereby inducing positive electron affinity (PEA) [20] and suppressing the desirable NEA properties.

To address these limitations, research has increasingly focused on surface terminations that combine the stability of oxygen-based systems with the dipole required for NEA. One promising approach involves metal–oxygen–carbon (M–O–C) configurations, where the metal (M) is selected based on its electronegativity difference with oxygen [11]. This arrangement enables the formation of a more complex dipole, arising from the combined contributions of the metal, oxygen, and carbon atoms. Several metals, including Li [28,29], Sc [30], Sn [31,32], Al and Ti [33], have been explored to tailor the electronic properties of diamond surfaces. These systems generally exhibit enhanced stability due to the stronger M–O and C—O bonds compared to C—H bonds.

Alternatively, direct metal termination of diamond surfaces through M–C (carbide) bond formation has also been investigated [17,34]. However, such systems tend to exhibit lower stability under light irradiation and air exposure, owing to the strong affinity of metals for oxygen, which promotes surface oxidation over carbide preservation.

In this work, we investigate the formation and characterization of FeO surface terminations on polycrystalline diamond (PCD). The synthesis is optimized and the surfaces are characterized by core-level and valence band photoemission spectroscopy at varying iron coverages on O-terminated PCD. We aim to determine how iron incorporation modifies the diamond band structure and whether the WF and NEA can be tuned through controlled deposition, using PCD as a scalable and technologically relevant alternative to single-crystal diamond (SCD). This approach is motivated by the substantial electronegativity difference between Fe (1.83) and O (3.44) [35,36], which suggests favourable conditions for dipole formation and makes iron a promising surface adsorbate.

2. Materials and methods

Freestanding boron-doped PCD substrates (product code: 145–500-0030) were purchased from Element Six Technologies Ltd. (Ascot, UK). Boron-doped diamond (BDD) was selected as the starting material because photoemission measurements require conductive substrates to avoid surface charging effects. According to the supplier specifications, the boron concentration is in the range of 2–6 $\times$ 10^{20} atoms/cm^3. The surface topography was subsequently characterized using a 3D laser scanning confocal microscope (Olympus LEXT), revealing an average surface roughness (R_a) better than 25 μm (Fig. S1 in Supporting Information). Laser Raman spectroscopy (Renishaw 2000) was also employed to investigate the structural quality and bonding characteristics of the diamond, with particular attention to the identification of sp^3 carbon features and possible defect-related contributions (Fig. S2).

Although the present study focuses on the macroscopic surface morphology characterized by 3D laser scanning confocal microscopy (Fig. S1), future studies employing tip-enhanced Raman spectroscopy (TERS), high-resolution transmission electron microscopy (TEM) or scanning tunneling microscopy (STM) could provide nanoscale insights into the relationship between local morphology, surface chemistry, and electronic properties.

Prior to use, the substrates were cleaned in a boiling acid mixture for 3 h to remove residual metal contamination from backside mechanical polishing, following Ref. [22]. After cleaning, O-termination was achieved by oxygen plasma treatment using the Tucano multipurpose plasma system from Gambetti Vacuum Technology. The plasma conditions were 100 W of forward power, 1.0 W of reflected power, −170.3 V of DC bias, an oxygen flow rate of 40.0 standard cubic centimetre (sccm) and a pressure of 6.9 $\times$ 10^{-1} mbar.

The sample was subsequently transferred into an UHV system, where metal deposition, thermal treatments and surface analysis were carried out without breaking vacuum. An annealing at 300 °C for 1 h was performed to remove adventitious carbon and water, further improving surface cleanliness [16,25,37]. Iron deposition was carried out by electron-beam physical vapor deposition (e-beam PVD) using an EBE-4 evaporator (SPECS GmbH) in the UHV preparation chamber. No crucible was used, since Fe was evaporated directly from a high-purity Fe rod (99.99 + %, Mateck GmbH) with a diameter of 2 mm, which served as the source material and was gradually heated to the target power over approximately 10 min. After a 10 min thermalization period at the target power, the deposition was initiated by opening a mechanical shutter. The sample was positioned approximately 20 cm away from the metal source and perpendicular to the metal flux to minimize shadowing effects. The deposition was performed at a voltage of 1079 V, a filament current of 2.8 A, and an emission current of 6.7 mA, corresponding to a power of 7.2 W. As described later, for the main results of this work, the sample temperature was kept constant at 230 °C during deposition.

The deposition rate was calibrated through a combination of photoemission measurements, primarily by monitoring the evolution of the Fe 2*p* core-level spectra as a function of deposition time. In particular, the relative contribution of metallic iron (i.e., non-reacted Fe on the surface) was used as an indicator of coverage: the absence of a metallic component corresponds to sub-monolayer coverage, whereas its increase indicates coverage exceeding one monolayer. Based on this analysis, one monolayer equivalent (MLE) of Fe is reached after ~10 min of deposition. Notably, additional photoemission results indicate a change in the electronic structure at 1.0 MLE, consistent with the attainment of a surface a saturation state (see in Section 3).

Core-level photoemission analyses were performed using X-ray photoemission spectroscopy (XPS) with a non-monochromatic Al Kα source (1486.7 eV). Spectra were acquired with pass energies of 50 eV for surveys and 20 eV for high-resolution measurements. Ultraviolet photoemission spectroscopy (UPS) measurements were carried out using a discharge lamp producing He(I) radiation (21.2 eV), with a pass energy of 2 eV. During UPS measurements, sample was biased at −25 V to enable accurate WF determination. The overall energy resolution of the UPS measurements was estimated to be ~0.1 eV, primarily limited by thermal broadening at room temperature. All spectra were acquired in normal-emission geometry and energy-referenced to the metallic Mo 3*d* core level (XPS) and the Fermi edge (UPS) of the sample holder. Measurements were performed using an ESCALAB MKII VG analyzer. XPS spectra were analyzed with XPSPEAK41 software (version 4.01) after Shirley background subtraction and fitted with Voigt line shapes, whereas UPS data were processed using Igor Pro (version 9.0). All relative component analyses for XPS were performed using the individual peak areas obtained from fitting, normalized to the total area determined by integrating the overall Shirley-background-subtracted peak envelope.

Since XPS and UPS measurements were performed in normal-emission geometry over a large analyzed area, the reported intensities, Fe coverages, WF values, and EA values should be interpreted as average surface properties of the rough pyramidal PCD surface (Fig. S1) rather than local values representative of an atomically flat surface.

3. Results and discussions

3.1. XPS characterization

The as-prepared O-terminated PCD surface was characterized by XPS to establish a reference for subsequent Fe deposition. Fig. 1(a,b) shows the deconvolution of the C 1*s* and O 1*s* core-level spectra of the O-terminated PCD, respectively, before and after each Fe deposition step. Survey spectra for each deposition are reported in Fig. S3.

For the O-terminated PCD, the main feature of the C 1*s* spectrum corresponds to the bulk C—C sp^3 component at a binding energy (BE) of

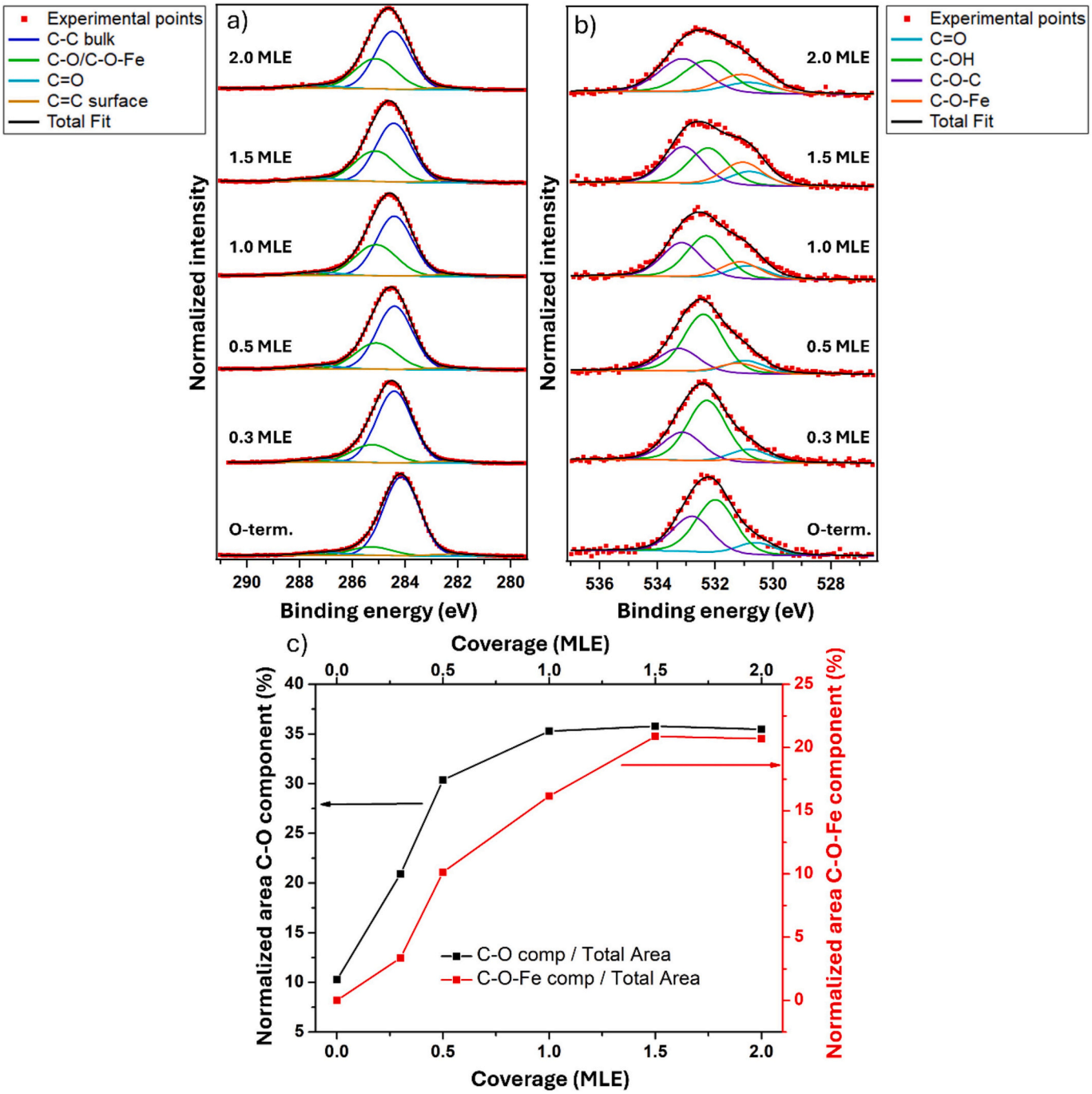

Fig. 1. Deconvolution of (a) C 1s and (b) O 1s spectra for each deposition step, obtained by peak fitting and normalized to the C 1s area. (c) Relative area of the C–O/C–O–Fe component in the C 1s (black) and the C–O–Fe component in the O 1s (red) as function of the coverage.

284.5 eV [29,38]. Oxidation is evidenced by two additional components at 285.7 eV and 287.4 eV, attributed to the C—O and C═O (carbonyl) groups [21]. A minor component (2%) at 282.2 eV is assigned to the sp^2 C—C bonds, expected on a PCD sample due to surface defect inherently present and generated by the doping process [24].

The O 1*s* spectrum can be deconvolved into three components at 530.6 eV, 532.0 eV and 532.8 eV, corresponding to the C═O, C-OH and C-O-C functional groups, respectively [22]. Among these, single bond carbon-oxygen species (C—O and C–O–C) represent the dominant contributions in both the C 1*s* and O 1*s* spectra. Stoichiometric analysis, based on the C—O component of the C 1*s* and the combined C–OH and C–O–C contributions of the O 1*s*, yields a composition of $CO_{0.78}$, after normalization using sensitivity factors. A comparable value of $CO_{0.80}$ is from O 1*s* analysis by accounting for one and two C atoms per C–OH and C–O–C group, respectively. This agreement supports the reliability of the spectral deconvolution and species assignment.

To investigate the behaviour of Fe deposited on the O-terminated PCD, a series of depositions was performed with increasing deposition times of 3, 5, 10, 15, and 20 min. These durations correspond to specific fractions of a monolayer, calibrated as described in Section 2, and are equivalent to 0.3, 0.5, 1.0, 1.5, and 2.0 MLEs, respectively. All depositions were carried out at a fixed sample temperature of 230 °C to ensure sufficient surface mobility of Fe atoms while minimizing changes in the sticking coefficient [39] and preventing desorption or modification of oxygen functional groups [21]. After each deposition step, the surface was characterized by XPS.

As shown in Fig. 1(a), the most prominent change upon Fe deposition is the progressive increase in the C—O component of the C 1*s* spectrum. This feature is therefore attributed not only to the original C—O groups but also to the formation of a new C–O–Fe contribution. The relative area of this component increases from around 10% for the O-terminated surface to ~35% after 1.0 MLE deposition, after which it stabilizes, indicating the attainment of a saturation regime (Fig. 1(c)). The complete evolution of peak areas is summarized in Table 1.

The assignment of a new C–O–Fe component, with a BE close to that of C—O, is supported by the fully in-situ synthesis and characterization under UHV conditions, where adsorption of additional O or C species is highly unlikely. The observed increase in the C—O peak is therefore related to the formation of this new contribution, which overlaps with the existing components and cannot be resolved within the experimental energy resolution. Furthermore, the increase in the C–O/C–O–Fe component is accompanied by a decrease in the sp^3 C—C bulk contribution, which originates from deeper regions of the material and is progressively attenuated by the deposited Fe overlayer [40].

In contrast, the O 1*s* spectrum exhibits the emergence of a distinct new component at 531.1 eV with increasing Fe coverage, as depicted in Fig. 1(b). Additionally, a systematic shift of the overall O 1*s* line toward higher BEs (~ +0.2–0.3 eV) is observed relative to the O-terminated PCD surface. This shift can be attributed to modifications of the surface dipole induced by Fe—O bond formation, characterized by an electronegativity difference of 1.61 (Pauling scale [35]), with the negative pole on the O and the positive pole on the Fe. The resulting outward-oriented dipole increases the energy required for electron emission, leading to a shift toward higher BEs.

Conversely, the C–O/C–O–Fe component in the C 1*s* core-level peak shifts toward lower BE (i.e., toward the sp^3 C—C bulk component). The separation between these two components decreases from +1.2 eV for the O-terminated surface to +0.7 eV at 1.0 MLE, remaining constant at higher coverages. This opposite shift behaviour between the C 1*s* and O 1*s* photoemission peaks is consistent with previous studies on diamond surface terminations, such as the transition from H- to O-terminated diamond [22,25,41] and signals a change in the electronic surface properties.

The electronegativity difference between Fe and O leads to significant charge transfer from Fe to O, influencing the BE of the C–O–Fe component in the O 1*s* peak. This component is located at approximately +0.3 eV and − 1.2 eV relative to the C═O and C–OH peaks, respectively. The higher electron-withdrawing capability of the C═O group arises from π bond delocalization, which concentrates electron density on the oxygen atom. In contrast, the C-OH group involves only a σ bond, lacking such delocalization. Although the Fe—O interaction results in substantial electron transfer to oxygen, this effect remains weaker than the π-delocalization in the carbonyl group. Consequently, the BE of oxygen in C–O–Fe lies between that of C═O (lower BE) and C–OH (higher BE).

With increasing Fe deposition, the relative area of the C–O–Fe peak increases from 3% after the first deposition step to about 16% at 1.0 MLE (Fig. 1(c)). Concurrently, the C–OH component decreases, while the combined area of C–OH and C–O–Fe remains nearly constant. This behaviour suggests that Fe preferentially reacts with C–OH sites, with minimal interaction with the more stable C–O–C and C═O functional groups.

Fig. 2(a) shows the deconvolution of the Fe 2*p* peak as a function of deposition. The fitting model focuses only the Fe $2p_{3/2}$ region and includes three components: two associated with iron oxide [42] and one with metallic iron [43]. At low coverages (0.3 and 0.5 MLE), only oxide-related components are observed, with BEs of 709.9 eV and 714.0 eV [42,44]. The absence of satellite features around 720 eV, together with the peak shape, indicates the predominance of Fe^{2+} species [44]. These results suggest that, at low coverages, deposited iron fully reacts with the oxygen-terminated surface to form specifically Fe^{2+}oxide.

At higher coverages, a metallic Fe component emerges at ~707.1 eV [44]. Its relative intensity increases nearly linearly with deposition time, as shown in Fig. 2(b), increasing from 2% at 1.0 MLE to 13% at 2.0 MLE. The observation that ~98% of iron is oxidized at 1.0 MLE supports the accuracy of the deposition calibration. Furthermore, the progressive increase of the metallic component is consistent with excess Fe forming an overlayer on top of the oxide, which no longer interacts with the substrate.

Stoichiometry analysis, based on the two oxide components of the Fe $2p_{3/2}$ spectrum and the C–O–Fe contribution in the O 1*s* peak, yields a composition close to $FeO_{0.96}$, confirming the presence of Fe^{2+} oxide on the surface. It is worth noting that the stabilization of Fe^{2+} at sub-monolayer coverage is a well-known phenomenon under UHV

Table 1
BEs and relative peak areas derived from the deconvolution of the C 1s and O 1s spectra.

C 1*s*				O 1*s*			
Sample	Component	BE (eV)	Relative peak area	Sample	Component	BE (eV)	Relative peak area (%)
O-term.	C-C sp^3 bulk	284.5	84	O-term.	C═O	530.6	13
	C-O	285.7	10		C-OH	532.0	54
	C═O	287.4	3		C-O-C	532.8	36
	C=C sp^2 surf	282.6	2		–	–	–
0.3 MLE	C-C sp^3 bulk	284.5	73	0.3 MLE	C═O	530.8	13
	C-O/C-O-Fe	285.4	21		C-OH	532.3	58
	C═O	287.5	4		C-O-C	533.1	27
	C=C sp^2 surf	282.7	2		C-O-Fe	531.1	3
0.5 MLE	C-C sp^3 bulk	284.5	64	0.5 MLE	C═O	531.0	13
	C-O/C-O-Fe	285.4	30		C-OH	532.4	57
	C═O	287.4	4		C-O-C	533.2	22
	C=C sp^2 surf	282.6	2		C-O-Fe	531.2	10
1.0 MLE	C-C sp^3 bulk	284.5	59	1.0 MLE	C═O	530.9	13
	C-O/C-O-Fe	285.2	35		C-OH	532.3	40
	C═O	287.4	4		C-O-C	533.2	34
	C=C sp^2 surf	282.6	2		C-O-Fe	531.1	16
1.5 MLE	C-C sp^3 bulk	284.5	59	1.5 MLE	C═O	530.8	13
	C-O/C-O-Fe	285.2	35		C-OH	532.2	32
	C═O	287.4	3		C-O-C	533.1	33
	C=C sp^2 surf	282.6	3		C-O-Fe	531.0	21
2.0 MLE	C-C sp^3 bulk	284.5	59	2.0 MLE	C═O	530.8	13
	C-O/C-O-Fe	285.2	35		C-OH	532.3	35
	C═O	287.4	3		C-O-C	533.1	36
	C=C sp^2 surf	282.6	2		C-O-Fe	531.1	21

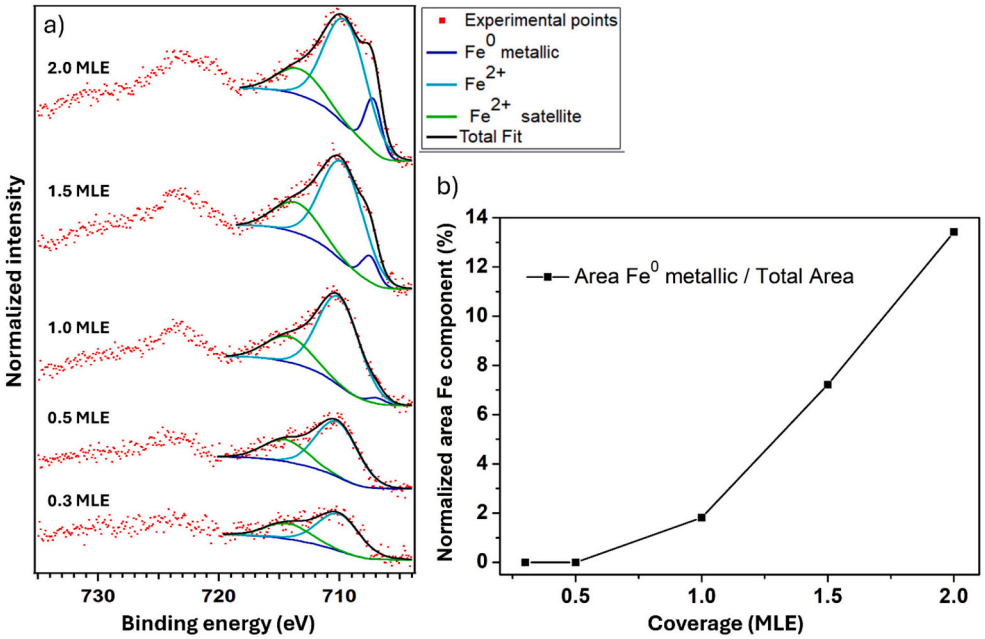

Fig. 2. (a) Deconvolution of Fe $2p_{3/2}$ peaks for each deposition step. (b) Relative area of the Fe^{0} metallic component as a function of the coverage.

conditions [42,45]. The FeO stoichiometry remains essentially constant even with the appearance of a metallic Fe component at 1.5 and 2.0 MLE. The only deviation is observed at 0.3 MLE, where the O: Fe ratio is ~0.5, indicating a sub-oxidized state. This behaviour can be attributed to the very low iron coverage, where over coordination with oxygen atoms may occur. Additionally, the low signal intensity at this deposition stage introduces higher uncertainty in the peak area determination.

Another important observation is that the emergence of metallic iron does not coincide with complete saturation of the O-terminated surface. In the O 1*s* core-level spectra at 1.0, 1.5, and 2.0 MLE, a residual C–OH component is still present in the deconvolution. This suggests that the surface is not uniformly covered by iron, likely due to the intrinsic roughness of the PCD substrate [46] Surface roughness and morphological irregularities may hinder uniform adsorption and limit Fe accessibility to all reactive sites. Furthermore, the diffusion of Fe atoms may be restricted by this complex surface morphology, and the mild thermal conditions during deposition may not be sufficient to overcome these limitations. Consistently, the C═O and C–O–C components appear largely unaffected by Fe deposition, indicating that portions of the surface remain unreacted.

Alternative strategies to improve the formation of the Fe oxide layer deposition were also investigated, as schematized in Fig. 3. In particular, the effect of substrate temperature during deposition was examined by performing Fe deposition on O-terminated PCD at room temperature.

A deposition time of 10 min was used, corresponding to approximately 1.0 MLE under the conditions of the main experiment (i.e., deposition at 230 °C). The resulting Fe 2*p* spectra are reported in Fig. S4.

Immediately after deposition, iron was predominantly in the metallic state, with a main component at ~707.3 eV, consistent with the formation of Fe nanoparticle agglomerates with limited contact with the O-terminated surface. Following annealing at 300 °C for 1 h under UHV, the dominant component shifted to FeO (~709.9 eV), although a non-negligible metallic contribution remained. This behaviour contrasts with the calibration obtained for deposition at 230 °C and can be attributed either to a higher sticking coefficient for Fe at room temperature [39] or to limited surface diffusion during post-annealing. Indeed, deposition on a heated substrate is generally more effective in promoting the uniform distribution of ultrathin overlayers compared to

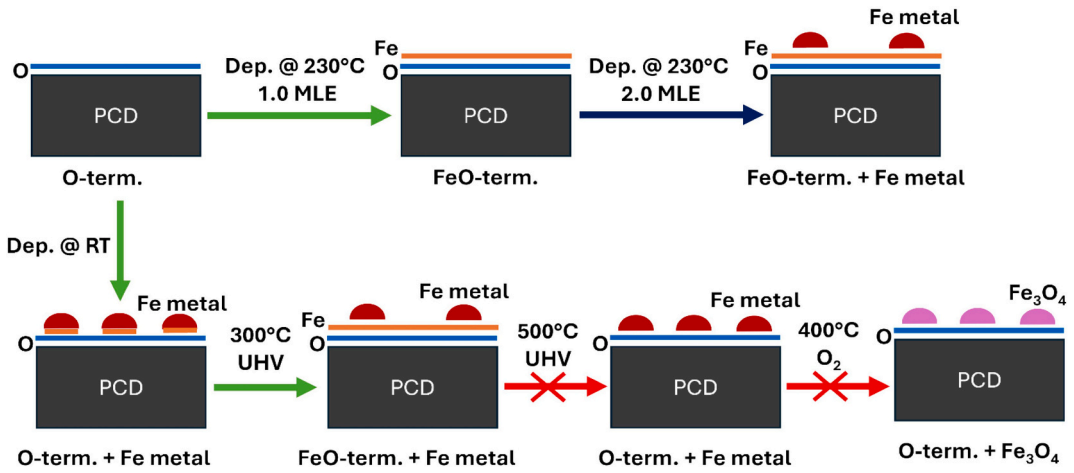

Fig. 3. Schematic summarizing the experimental steps. The upper row shows the results of stepwise deposition performed at 230 °C, while the lower row presents the treatment steps carried out after deposition at room temperature.

post-deposition annealing [47].

Further annealing at 500 °C for 1 h under UHV was performed to enhance Fe mobility and promote reaction with additional oxygen functionalities. However, this treatment led to an increase in the metallic component, suggesting a reduction of FeO and agglomeration into metallic Fe nanoparticles. An additional annealing step at 400 °C under an oxygen partial pressure of 5.2×10^{-6} mbar for 1 h was carried out to re-oxidize the metallic iron. As shown in Fig. S4, the Fe 2*p* peak shifted to higher BE (~710.8 eV), characteristic of Fe_3O_4 [44]. This indicates that oxygen exposure promotes oxidation of Fe clusters, leading to the formation of magnetite islands rather than restoring the Fe^{2+} oxide phase.

These results demonstrate that controlled formation of the Fe–O–C termination is best achieved by depositing Fe on a heated substrate (~230 °C) while limiting the coverage to 1.0 MLE to avoid the formation of metallic Fe overlayers. Alternatively, a similar composition can be obtained by deposition at room temperature followed by post-annealing at 300 °C, as indicated by the green arrows in Fig. 3. Other deposition conditions may also lead to different results, for example, by employing an atomic oxygen source capable of oxidizing both Fe and the diamond surface [25]. However, this would introduce a much wider parameter space, whereas the approach based on Fe deposition at 230 °C provides an efficient and straightforward route to obtain the desired FeO-like surface termination.

3.2. Electronic structure

The electronic structure of the sample was characterized by UPS at each stage of the experiment. As for the surface analysis, the pristine O-terminated PCD was first measured as a benchmark for subsequent iron deposition. The valence band maximum (VBM) was determined by linear extrapolation of the leading edge of the valence band (VB) toward the Fermi level [17,29,30]. Although the absolute WF values may be affected by the local surface roughness [48], the deposition of ultrathin films does not alter the macroscopic features of the PCD surface (Fig. S1). Therefore, the roughness remains macroscopically comparable

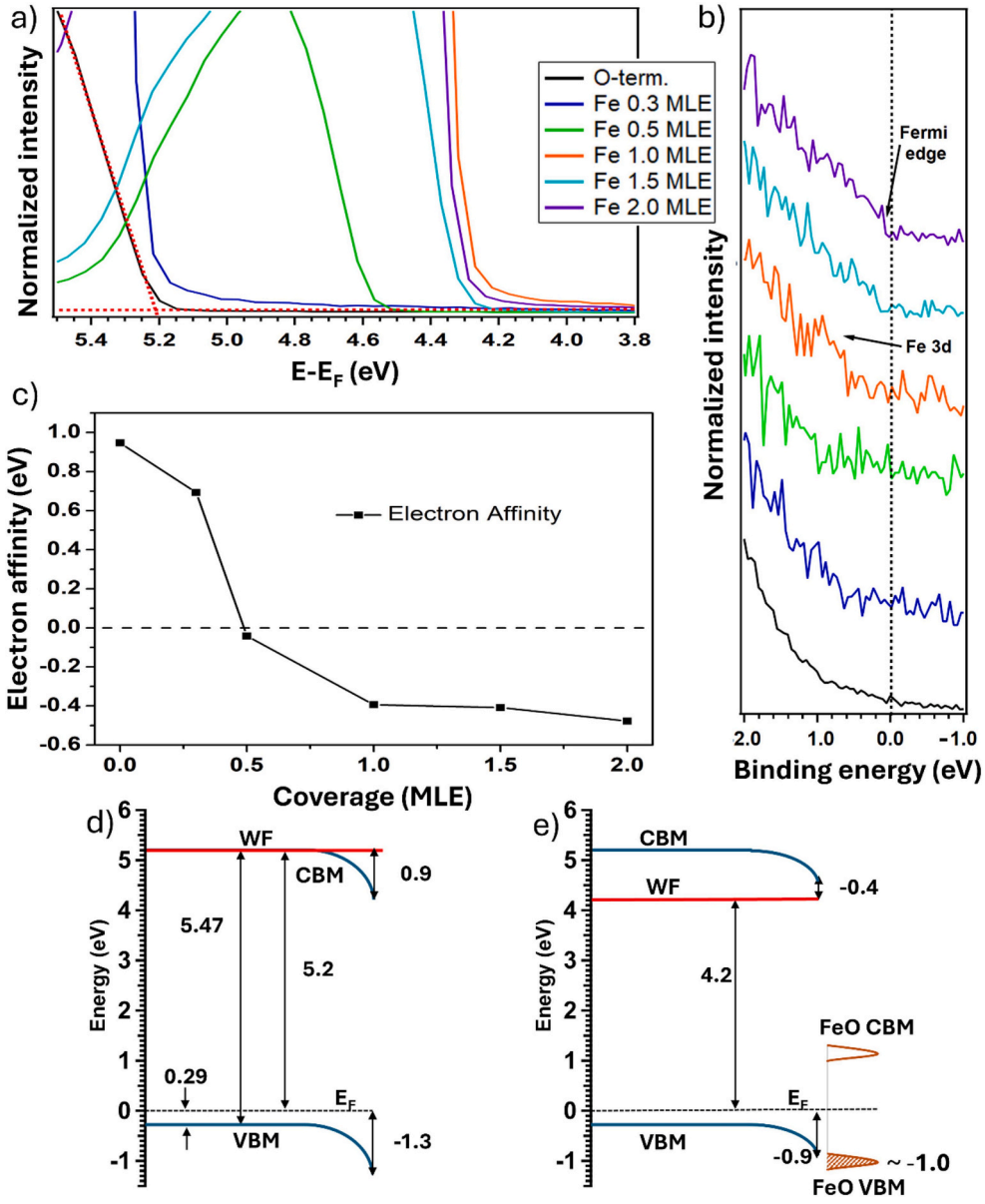

Fig. 4. (a) Work function determination, with dotted lines illustrating the linear extrapolation. (b) Valence band maximum (VBM) region, showing the Fe 3d state at ~1.0 eV BE for 1.0 MLE coverage; spectra are normalized at 3 eV. (c) Electron affinity as a function of coverage. Schematic energy level diagram of (d) O-terminated PCD and (e) the 1.0 MLE Fe-deposited O-terminated PCD sample, with FeO states indicated.

across the investigated samples, and the differences observed after the different treatments reflect real changes in the sample photoemission response.

The WF was extracted from the difference between the secondary electron cut-off and the excitation energy of the ultraviolet source (21.2 eV), as illustrated in Fig. 4(a). While the determination of the WF is relatively straightforward due to the well-defined cut-off, the extraction of the VBM is less precise, as the valence band edge does not exhibit a sharp onset.

The CBM was then estimated using the diamond band gap of 5.47 eV [17,30]. Consequently, the electron affinity (EA) was calculated as the difference between the WF and the CBM. The relationship used for this calculation is reported in Eq. (1), as follows:

$$EA = WF - (VBM + E_g) \quad (1)$$

The resulting electronic structure values, including WF, VBM, CBM and EA are summarized in Table 2.

Fig. 4(c) shows the progressive reduction of the EA, leading to the onset of NEA as a function of Fe coverage. The O-terminated PCD sample exhibits PEA of +0.9 eV, with a WF of 5.2 eV relative to the Fermi level, in good agreement with the literature [22]. Upon iron deposition, the sample progressively transitions from PEA to NEA, with EA decreasing from +0.7 eV at 0.3 MLE (WF = 5.2 eV) to −0.4 eV at 1.0 MLE (WF = 4.2 eV).

At 0.5 MLE, the EA reaches a slightly negative value (−0.04 eV), which is within the experimental uncertainty. Although this coverage is insufficient to fully induce NEA, the formation of Fe–O–C dipoles significantly reduces the EA of the O-terminated surface. This behaviour is consistent with the XPS results, including the evolution of the C–O–Fe component and the formation of FeO stoichiometry. At 1.0 MLE, a stable NEA of −0.4 eV is achieved, corresponding to a WF of 4.2 eV. Beyond this coverage, the WF remains essentially unchanged, in agreement with XPS observations indicating surface saturation. At higher coverages (>1.0 MLE), excess iron remains in metallic form and does not contribute to additional Fe–O–C dipoles, thus limiting further reduction of the WF.

As shown in Fig. 4(b) and highlighted in Fig. S5, a new feature at ~1.0 eV BE emerges from 1.0 MLE and is attributed to Fe 3*d* states of the FeO layer [49,50]. This indicates that the oxide layer retains its intrinsic electronic structure while modifying the diamond surface properties. FeO is a semiconductor with a band gap in the range of 2.0–2.4 eV in bulk [51–53] and ~ 2.12 eV in monolayer form [54]. The presence of a well-defined Fe 3*d* state suggests the formation of a semiconductor-semiconductor junction at the interface, which is crucial for tuning the electronic properties of the system. [33]

At 2.0 MLE, a clear electron density at the Fermi level is observed, confirming the presence of metallic Fe. Although the metallic component is not dominant in XPS (recall Fig. 2), it is clearly detected by UPS due to its higher surface sensitivity, indicating that the metallic Fe forms an overlayer on top of the oxide [55]. At 1.5 MLE, intermediate states between 0 and 2 eV are observed, corresponding to a mixture of FeO and metallic Fe contributions (see Fig. 4 and S5).

The VBM shifts from 1.3 eV for the O-terminated PCD surface to 1.0 eV at 0.3 MLE, further decreasing to 0.9 eV at intermediate coverages and reaching 0.8 eV at 2.0 MLE. It should be noted that the uncertainty in VBM and EA increases at higher coverages due to the abovementioned overlap between metallic and oxide features.

Assuming a pinned bulk Fermi level located 0.29 eV above the VBM for heavily boron-doped diamond, as reported by Maier et al. [18], the surface band bending can be estimated to range from 0.9 to 0.6 eV. Fig. 4 (d) illustrates the band alignment for the O-terminated surface and the 1.0 MLE sample, respectively, highlighting both the band bending and the shift of the WF below the CBM in the NEA regime. Fig. 4(d) also illustrates the occupied and unoccupied states of the FeO layer. While occupied states are directly observed in UPS [16], the unoccupied states are inferred by adding 2.12 eV [54] to the filled state. This results in well-defined in-gap states, which are of particular interest for future applications, such as photocatalysis and electron emission processes [56].

Overall, UPS results are consistent with XPS findings, confirming that a coverage of ~1.0 MLE produces the most significant modification of the electronic structure. The enhanced NEA at 1.0 MLE is further evidenced by integrating the UPS spectra (Fig. S6), normalized to the diamond features at ~3 and ~ 8 eV, showing a 9–10-fold increase in photoemission intensity compared to the O-terminated surface.

Table 2
Summary of electron structure values obtained from the UPS analysis.

Sample	VBM (eV)	WF (eV)	CBM (eV)	EA (eV)
O-term.	−1.3	5.2	4.2	0.9
0.3 MLE	−1.0	5.2	4.5	0.7
0.5 MLE	−0.9	4.5	4.5	0.0 (−0.04)
1.0 MLE	−0.9	4.2	4.6	−0.4
1.5 MLE	−0.9	4.2	4.6	−0.4
2.0 MLE	−0.8	4.2	4.7	−0.5

4. Conclusions

We report the preparation and photoelectron spectroscopy characterization of a novel FeO-terminated PCD surface. Among the investigated growth strategies, deposition at 230 °C proved to be the most effective, enabling a systematic study of the electronic properties as a function of Fe coverage. Iron preferentially reacts with surface hydroxyl (–OH) groups, leading to the formation of an Fe^{2+} oxide layer. At low coverage (0.3 MLE), the resulting dipole density is insufficient to significantly modify the surface electronic structure, whereas at 0.5 MLE pronounced band bending and a substantial reduction in EA are observed. The optimal modification is achieved at 1.0 MLE, where the WF reaches a minimum value of 4.2 eV, and the EA becomes negative (−0.4 eV). Further increases in Fe coverage do not improve the surface properties, as excess iron remains in metallic form and does not contribute to additional Fe–O–C dipole formation.

At 1.0 MLE, UPS measurements reveal Fe 3*d* states at ~1.0 eV, consistent with FeO formation, and indicate the emergence of a semiconductor-semiconductor interface. To the best of our knowledge, this is the first observation of oxide-specific electronic states in UPS for an M–O–C-terminated diamond surface. These results demonstrate that controlled Fe–O–C interfacial engineering enables the induction and tuning of NEA in diamond. The FeO–diamond system, combining interfacial electronic states with NEA, represents a promising platform for photocatalytic and electron emission applications under visible light.

The FeO-termination demonstrates the ability to induce NEA under controlled conditions; however, further dedicated investigations of its long-term environmental and high-temperature stability are required to assess its robustness under realistic operating conditions and its potential for future applications. In addition, further electrical and nanoscale characterization, for example by conductive AFM or STM on well-defined SCD substrates, will be important to clarify the role of residual metallic Fe and thicker Fe-containing layers in the surface conductivity and local electronic properties of the FeO/diamond interface.

CRediT authorship contribution statement

Ettore Mingardo: Writing – review & editing, Writing – original draft, Visualization, Methodology, Investigation, Formal analysis, Data curation. **Ramiz Zulkharnay:** Writing – review & editing, Writing – original draft, Validation, Supervision, Methodology, Investigation, Funding acquisition. **Mattia Cattelan:** Writing – review & editing, Writing – original draft, Visualization, Validation, Supervision, Resources, Project administration, Methodology, Investigation, Funding acquisition, Formal analysis, Data curation, Conceptualization.

Declaration of competing interest

The authors declare that they have no known competing financial interests or personal relationships that could have appeared to influence the work reported in this paper.

Acknowledgments

MC acknowledges the University of Padova for financial support through the BIRD 2025 P-DiSC project "TiDEN" (P-DiSC#08BIRD2025-UNIPD) and the STARS@UNIPD 2025 CoG project "SOLVENIRE", supported by the STARS@UNIPD 2025 programme with the contribution of Fondazione Cassa di Risparmio di Padova e Rovigo. RZ wishes to acknowledge funding support from the Royal Society of Chemistry through a Researcher Collaborations Grant (C25-8928513904) and a Sustainable Laboratories Grant (L25-7399277638).

Appendix A. Supplementary data

Supplementary data to this article can be found online at https://doi.org/10.1016/j.diamond.2026.113985.

Data availability

Data will be made available on request.

References

[1] R. Zulkharnay, P.W. May, Applications of diamond films: a review, Functional Diamond 4 (2024), https://doi.org/10.1080/26941112.2024.2410160.
[2] K.A.A. Khalid, T.J. Leong, K. Mohamed, Review on thermionic energy converters, IEEE Trans. Electron Devices 63 (2016) 2231–2241, https://doi.org/10.1109/TED.2016.2556751.
[3] D.M. Trucchi, A. Bellucci, M. Girolami, P. Calvani, E. Cappelli, S. Orlando, R. Polini, L. Silvestroni, D. Sciti, A. Kribus, Solar thermionic-thermoelectric generator (ST2G): concept, materials engineering, and prototype demonstration, Adv. Energy Mater. 8 (2018), https://doi.org/10.1002/aenm.201802310.
[4] G.R. Mackenzie, S. Kaluvan, P.G. Martin, C. Hutson, T. Connolley, M. Cattelan, H. Dominguez-Andrade, T.L. Martin, N.A. Fox, T.B. Scott, A diamond gammavoltaic cell utilizing surface conductivity and its response to different photon interaction mechanisms, Mater. Today Energy 21 (2021), https://doi.org/10.1016/j.mtener.2021.100688.
[5] A. Shih, J. Yater, P. Pehrsson, J. Butler, C. Hor, R. Abrams, Secondary electron emission from diamond surfaces, J. Appl. Phys. 82 (1997) 1860–1867, https://doi.org/10.1063/1.365990.
[6] A. Aleksov, M. Kubovic, N. Kaeb, U. Spitzberg, A. Bergmaier, G. Dollinger, T. Bauer, M. Schreck, B. Stritzker, E. Kohn, Diamond field effect transistors—concepts and challenges, Diamond Relat. Mater. 12 (2003) 391–398, https://doi.org/10.1016/S0925-9635(02)00401-6.
[7] K. Okano, S. Koizumi, S.R.P. Silva, G.A.J. Amaratunga, Low-threshold cold cathodes made of nitrogen-doped chemical-vapour-deposited diamond, Nature 381 (1996) 140–141, https://doi.org/10.1038/381140a0.
[8] M. Cattelan, Diamond-based solvated electron generators: a perspective on applications in NRR, CO2RR, and pollutant degradation, Solids 6 (2025) 24, https://doi.org/10.3390/solids6020024.
[9] D. Zhu, L. Zhang, R.E. Ruther, R.J. Hamers, Photo-illuminated diamond as a solid-state source of solvated electrons in water for nitrogen reduction, Nat. Mater. 12 (2013) 836–841, https://doi.org/10.1038/nmat3696.
[10] L. Zhang, R.J. Hamers, Photocatalytic reduction of CO2 to CO by diamond nanoparticles, Diamond Relat. Mater. 78 (2017) 24–30, https://doi.org/10.1016/j.diamond.2017.07.005.
[11] M.C. James, F. Fogarty, R. Zulkharnay, N.A. Fox, P.W. May, A review of surface functionalisation of diamond for thermionic emission applications, Carbon N. Y. 171 (2021) 532–550, https://doi.org/10.1016/j.carbon.2020.09.019.
[12] R.J. Nemanich, P.K. Baumann, M.C. Benjamin, S.W. King, J. Van Der Weide, R. F. Davis, Negative electron affinity surfaces of aluminum nitride and diamond, Diamond Relat. Mater. 5 (1996) 790–796, https://doi.org/10.1016/0925-9635(95)00485-8.
[13] K.P. Loh, M. Nishitani-Gamo, I. Sakaguchi, T. Taniguchi, T. Ando, Thermal stability of the negative electron affinity condition on cubic boron nitride, Appl. Phys. Lett. 72 (1998) 3023–3025, https://doi.org/10.1063/1.121528.
[14] D. Takeuchi, S.-G. Ri, H. Kato, C.E. Nebel, S. Yamasaki, Negative electron affinity on hydrogen terminated diamond, Phys. Status Solidi A 202 (2005) 2098–2103, https://doi.org/10.1002/pssa.200561927.
[15] J. van der Weide, Z. Zhang, P.K. Baumann, M.G. Wensell, J. Bernholc, R. J. Nemanich, Negative-electron-affinity effects on the diamond (100) surface, Phys. Rev. B 50 (1994) 5803–5806, https://doi.org/10.1103/PhysRevB.50.5803.
[16] G. Wan, A. Croot, N.A. Fox, M. Cattelan, Empty-State Band Mapping Using Momentum-Resolved Secondary Electron Emission, Adv. Funct. Mater. 31 (2021), https://doi.org/10.1002/adfm.202007319.
[17] R. Zulkharnay, P.W. May, Experimental evidence for large negative electron affinity from scandium-terminated diamond, J. Mater. Chem. A Mater. 11 (2023) 13432–13445, https://doi.org/10.1039/d2ta09199b.
[18] F. Maier, J. Ristein, L. Ley, Electron affinity of plasma-hydrogenated and chemically oxidized diamond (100) surfaces, Phys. Rev. B Condens. Matter Mater. Phys. 64 (2001), https://doi.org/10.1103/PhysRevB.64.165411.
[19] H. Dominguez-Andrade, J. Anaya, A. Croot, M. Cattelan, D.J. Twitchen, M. Kuball, N.A. Fox, Correlating thermionic emission with specific surface reconstructions in a hydrogenated single-crystal diamond, ACS Appl. Mater. Interfaces 12 (2020) 26534–26542, https://doi.org/10.1021/acsami.0c01677.
[20] M. Tachiki, Y. Kaibara, Y. Sumikawa, M. Shigeno, H. Kanazawa, T. Banno, K. Soup Song, H. Umezawa, H. Kawarada, Characterization of locally modified diamond surface using Kelvin probe force microscope, Surf. Sci. 581 (2005) 207–212, https://doi.org/10.1016/j.susc.2005.02.054.
[21] N. Dontschuk, L.V.H. Rodgers, J.P. Chou, D.A. Evans, K.M. O'Donnell, H. J. Johnson, A. Tadich, A.K. Schenk, A. Gali, N.P. de Leon, A. Stacey, X-ray quantification of oxygen groups on diamond surfaces for quantum applications, Mater. Quantum Technol. 3 (2023) 045901, https://doi.org/10.1088/2633-4356/ad001b.
[22] R. Zulkharnay, G. Zulpukarova, P.W. May, Oxygen-terminated diamond: insights into the correlation between surface oxygen configurations and work function values, Appl. Surf. Sci. 658 (2024), https://doi.org/10.1016/j.apsusc.2024.159776.
[23] F. Klauser, S. Ghodbane, R. Boukherroub, S. Szunerits, D. Steinmüller-Nethl, E. Bertel, N. Memmel, Comparison of different oxidation techniques on single-crystal and nanocrystalline diamond surfaces, Diamond Relat. Mater. 19 (2010) 474–478, https://doi.org/10.1016/j.diamond.2009.11.013.
[24] X. Wang, A.R. Ruslinda, Y. Ishiyama, Y. Ishii, H. Kawarada, Higher coverage of carboxylic acid groups on oxidized single crystal diamond (001), Diamond Relat. Mater. 20 (2011) 1319–1324, https://doi.org/10.1016/j.diamond.2011.08.011.
[25] G. Wan, M. Cattelan, N.A. Fox, Electronic structure tunability of diamonds by surface functionalization, J. Phys. Chem. C 123 (2019), https://doi.org/10.1021/acs.jpcc.8b11232.
[26] C. Li, X. Zhang, E.F. Oliveira, A.B. Puthirath, M.R. Neupane, J.D. Weil, A. G. Birdwell, T.G. Ivanov, S. Kong, T. Gray, H. Kannan, A. Biswas, R. Vajtai, D. S. Galvao, P.M. Ajayan, Systematic comparison of various oxidation treatments on diamond surface, Carbon N. Y. 182 (2021) 725–734, https://doi.org/10.1016/j.carbon.2021.06.050.
[27] N. Tokuda, H. Umezawa, S.-G. Ri, K. Yamabe, H. Okushi, S. Yamasaki, Roughening of atomically flat diamond (111) surfaces by a hot HNO_3/H_2SO_4 solution, Diamond Relat. Mater. 17 (2008) 486–488, https://doi.org/10.1016/j.diamond.2008.01.042.
[28] S. Ullah, L. Cullingford, T. Zhang, J.R. Wong, G. Wan, M. Cattelan, N. Fox, An investigation into the surface termination and near-surface bulk doping of oxygen-terminated diamond with lithium at various annealing temperatures, MRS Adv. 6 (12) (2021) 311–320, https://doi.org/10.1557/s43580-021-00060-x.
[29] R. Zulkharnay, W. Greenwood, A. Wood, J. Laverock, N.A. Fox, Achieving a Large Net "Negative Electron Affinity" on Diamond (100) via Molecular Oxygen and Lithium Functionalization, ACS Appl. Mater. Interfaces 18 (2026) 9032–9042, https://doi.org/10.1021/acsami.5c20029.
[30] R. Zulkharnay, N.A. Fox, P.W. May, Enhanced Electron Emission Performance and Air-Surface Stability in ScO-Terminated Diamond for Thermionic Energy Converters, Small 20 (2024), https://doi.org/10.1002/smll.202405408.
[31] S. Ullah, N. Fox, Modification of the Surface Structure and Electronic Properties of Diamond (100) with Tin as a Surface Termination: A Density Functional Theory Study, J. Phys. Chem. C 125 (2021) 25165–25174, https://doi.org/10.1021/acs.jpcc.1c05973.
[32] G. Xiao, G. Zheng, M. Qiu, Q. Li, D. Li, M. Ni, Structure and electronic properties of tin monoxide (SnO) and lithiated SnO terminated diamond (100) and its comparison with lithium oxide terminated diamond, Appl. Surf. Sci. 559 (2021) 149962, https://doi.org/10.1016/j.apenergy.2017.09.021.
[33] M.C. James, M. Cattelan, N.A. Fox, R.F. Silva, R.M. Silva, P.W. May, Experimental studies of electron affinity and work function from aluminium on oxidized diamond (100) and (111) surfaces, Physica Status Solidi (B) 258 (2021) 2100027, https://doi.org/10.1002/pssb.202100027.
[34] A.K. Tiwari, J.P. Goss, P.R. Briddon, N.G. Wright, A.B. Horsfall, M.J. Rayson, Electronic and structural properties of diamond (001) surfaces terminated by selected transition metals, Phys. Rev. B 86 (2012) 155301, https://doi.org/10.1103/PhysRevB.86.155301.
[35] Electronegativity | Periodic Table of Elements - PubChem, (n.d.). https://pubchem.ncbi.nlm.nih.gov/ptable/electronegativity/ (accessed March 27, 2026).
[36] L. Pauling, J.C. Slater, F. Hund, The nature of the chemical bond. IV. The energy of single bonds and the relative electronegativity of atoms, J. Am. Chem. Soc. 54 (2002) 3570–3582, https://doi.org/10.1021/ja01348a011.
[37] G. Wan, S. Panditharatne, N.A. Fox, M. Cattelan, Graphene-diamond junction photoemission microscopy and electronic interactions, Nano Express 1 (2020), https://doi.org/10.1088/2632-959X/aba443.
[38] S. Ghodbane, D. Ballutaud, A. Deneuville, C. Baron, Influence of boron concentration on the XPS spectra of the (100) surface of homoepitaxial boron-doped diamond films, Physica Status Solidi (A) 203 (2006) 3147–3151, https://doi.org/10.1002/pssa.200671123.

[39] D.Y. Lenev, G.E. Norman, Sticking coefficient for Fe atoms interacting with iron cluster, in: J. Phys. Conf. Ser, Institute of Physics Publishing, 2018, https://doi.org/10.1088/1742-6596/946/1/012111.
[40] D. Petrini, K. Larsson, A theoretical study of the energetic stability and geometry of hydrogen- and oxygen-terminated diamond (100) surfaces, J. Phys. Chem. C 111 (2006) 795–801, https://doi.org/10.1021/jp063383h.
[41] L. Diederich, O.M. Küttel, P. Aebi, L. Schlapbach, Electron affinity and work function of differently oriented and doped diamond surfaces determined by photoelectron spectroscopy, Surf. Sci. 418 (1998) 219–239, https://doi.org/10.1016/S0039-6028(98)00718-3.
[42] J. Yang, E. Ascrizzi, M. Cattelan, M. Nalesso, L. Cielo, P. Matvija, F. Sedona, A. M. Ferrari, S. Agnoli, Atomic-Scale View of Water Chemistry on Nanostructured Iron Oxide Films, Nano Lett. 24 (2024) 12552–12559, https://doi.org/10.1021/acs.nanolett.4c03521.
[43] M. Bissoli, C.M.G. de Faria, V. Torresan, M.A. Lacavalla, M. Cattelan, D. Badocco, P. Pastore, P. Marzola, L. Cansolino, C. Ferrari, I. Postuma, R. Vago, S. Bortolussi, A.E. Spinelli, D. Forrer, V. Amendola, Taming the immiscibility of gold, iron, and boron to craft chemodegradable nanoparticles for multimodal imaging and radiotherapy, Adv. Healthc. Mater. (2026) e05031, https://doi.org/10.1002/adhm.202505031.
[44] M.C. Biesinger, B.P. Payne, A.P. Grosvenor, L.W.M. Lau, A.R. Gerson, R.S.C. Smart, Resolving surface chemical states in XPS analysis of first row transition metals, oxides and hydroxides: Cr, Mn, Fe, Co and Ni, Appl. Surf. Sci. 257 (2011) 2717–2730, https://doi.org/10.1016/j.apsusc.2010.10.051.
[45] H.C. Galloway, J.J. Benítez, M. Salmeron, The structure of monolayer films of FeO on Pt(111), Surf. Sci. 298 (1993) 127–133, https://doi.org/10.1016/0039-6028(93)90089-3.
[46] S. Veljković, V. Mitić, V. Paunović, G. Lazović, M. Mohr, H. Fecht, Analyses of the surface parameters in polycrystalline diamonds, Serb. J. Electr. Eng. 17 (2020) 111–129, https://doi.org/10.2298/SJEE2001111V.
[47] M. Cattelan, B. Markman, G. Lucchini, P.K. Das, I. Vobornik, J.A. Robinson, S. Agnoli, G. Granozzi, New strategy for the growth of complex heterostructures based on different 2D materials, Chem. Mater. 27 (2015) 4105–4113, https://doi.org/10.1021/acs.chemmater.5b01170.
[48] J.W. Kim, A. Kim, H.U. Hwang, J.H. Kim, S. Choi, N. Koch, D. Shin, Z. Zhao, F. Liu, M. Choi, K.M. Lee, Y. Park, Work function measurement by ultraviolet photoelectron spectroscopy: Versailles project on advanced materials and standards interlaboratory study, J. Vac. Sci. Technol. A 41 (2023), https://doi.org/10.1116/6.0002852.
[49] P.M. Düring, P. Rosenberger, L. Baumgarten, F. Alarab, F. Lechermann, V. N. Strocov, M. Müller, Tunable 2D electron- and 2D hole states observed at Fe/SrTiO3 interfaces, Adv. Mater. 36 (2024) 2309217, https://doi.org/10.1002/adma.202309217.
[50] R. Sakakibara, T.o. Terasawa, T. Kawauchi, K. Fukutani, T. Ito, W. Norimatsu, 2D iron oxide at the graphene/SiC(0001) interface, Small Methods (2026) e01889, https://doi.org/10.1002/smtd.202501889.
[51] R. Ashraf, S. Riaz, M. Saeed Akhtar, S. Naseem, Study of Structural and Electronic Properties of Iron Oxide by ADF, n.d.
[52] T. Eom, H.K. Lim, W.A. Goddard, H. Kim, First-principles study of iron oxide polytypes: comparison of GGA+U and hybrid functional method, J. Phys. Chem. C 119 (2014) 556–562, https://doi.org/10.1021/jp508096b.
[53] J. Dong, X.W. Yan, F. Ma, Strongly correlated electronic properties of FeO studied by the SCAN+U functional, J. Phys. Chem. C 127 (2023) 5513–5518, https://doi.org/10.1021/acs.jpcc.2c07961.
[54] K.V. Larionov, D.G. Kvashnin, P.B. Sorokin, 2D FeO: a new member in 2D metal oxide family, J. Phys. Chem. C 122 (2018) 17389–17394, https://doi.org/10.1021/acs.jpcc.8b06054.
[55] A. Szczepanska, G. Wan, M. Cattelan, N.A. Fox, N. Vasiljevic, Surface investigation on electrochemically deposited lead on gold, Surfaces 2 (2019) 56–68, https://doi.org/10.3390/surfaces2010006.
[56] C. Saucedo, N. Rieders, R.J. Hamers, Influence of hydrogen and oxygen surface termination on the mechanism of sub-bandgap photoelectron emission from diamond(111) into vacuum and into water, Diamond Relat. Mater. 153 (2025) 112011, https://doi.org/10.1016/j.diamond.2025.112011.